NASA/TM – 20220018456

Fabrication and Testing of a Novel Ceramic-Based Additively Manufactured Humidity Sensor

K.R. Hanekom and T.D. Rolin
Marshall Space Flight Center, Huntsville, Alabama

December 2022

The NASA STI Program…in Profile

Since its founding, NASA has been dedicated to the advancement of aeronautics and space science. The NASA Scientific and Technical Information (STI) Program Office plays a key part in helping NASA maintain this important role.

The NASA STI Program Office is operated by Langley Research Center, the lead center for NASA's scientific and technical information. The NASA STI Program Office provides access to the NASA STI Database, the largest collection of aeronautical and space science STI in the world. The Program Office is also NASA's institutional mechanism for disseminating the results of its research and development activities. These results are published by NASA in the NASA STI Report Series, which includes the following report types:

- TECHNICAL PUBLICATION. Reports of completed research or a major significant phase of research that present the results of NASA programs and include extensive data or theoretical analysis. Includes compilations of significant scientific and technical data and information deemed to be of continuing reference value. NASA's counterpart of peer-reviewed formal professional papers but has less stringent limitations on manuscript length and extent of graphic presentations.

- TECHNICAL MEMORANDUM. Scientific and technical findings that are preliminary or of specialized interest, e.g., quick release reports, working papers, and bibliographies that contain minimal annotation. Does not contain extensive analysis.

- CONTRACTOR REPORT. Scientific and technical findings by NASA-sponsored contractors and grantees.

- CONFERENCE PUBLICATION. Collected papers from scientific and technical conferences, symposia, seminars, or other meetings sponsored or cosponsored by NASA.

- SPECIAL PUBLICATION. Scientific, technical, or historical information from NASA programs, projects, and mission, often concerned with subjects having substantial public interest.

- TECHNICAL TRANSLATION. English-language translations of foreign scientific and technical material pertinent to NASA's mission.

Specialized services that complement the STI Program Office's diverse offerings include creating custom thesauri, building customized databases, organizing and publishing research results…even providing videos.

For more information about the NASA STI Program Office, see the following:

- Access the NASA STI program home page at <http://www.sti.nasa.gov>

- E-mail your question via the Internet to <help@sti.nasa.gov>

- Phone the NASA STI Help Desk at 757–864–9658

- Write to:
  NASA STI Information Desk
  Mail Stop 148
  NASA Langley Research Center
  Hampton, VA 23681–2199, USA

NASA/TM – 20220018456

Fabrication and Testing of a Novel Ceramic-Based Additively Manufactured Humidity Sensor

K.R. Hanekom and T.D. Rolin
Marshall Space Flight Center, Huntsville, Alabama

National Aeronautics and
Space Administration

Marshall Space Flight Center • Huntsville, Alabama 35812

December 2022

TRADEMARKS

Available from:

NASA STI Information Desk
Mail Stop 148
NASA Langley Research Center
Hampton, VA 23681–2199, USA
757–864–9658

This report is also available in electronic form at
<http://www.sti.nasa.gov>

TABLE OF CONTENTS

LIST OF FIGURES

LIST OF FIGURES (Continued)

LIST OF TABLES

LIST OF ACRONYMS AND SYMBOLS

AC	alternating current
Ag	silver
AM	additive manufacturing
B	lanthanum-doped barium titanate + 1 wt.% potassium hydroxide
Ba	barium
$BaTiO_3$	barium titanate
Bi	bismuth
C	carbon
CD	coarse dielectric
Cl	chlorine
Cs	cesium
DC	direct current
E	epoxy
FD	fired dielectric
FF	freshly formed
H	hydrogen
I	iodine
ISS	International Space Station
K	potassium
KOH	potassium hydroxide

LIST OF ACRONYMS AND SYMBOLS (Continued)

La	lanthanum
Li	lithium
MD	milled dielectric
Mo	molybdenum
MPOSS	mercaptopropyl polyhedral oligo-meric silsesquioxane
MSFC	Marshall Space Flight Center
Na	sodium
Nb	niobium
O	oxygen; Dextrol OC-40
OM	order of magnitude
Pb	lead
PD	pressed dielectric
PPC	parallel place capacitor
R	resin
RH	relative humidity
rLBT	reduced lanthanum barium titanate
S	sulfur; Stepfac 8180
SBA-15	Santa Barbara Amorphous-15
Sn	tin
Ti	titanium
UV	ultraviolet

LIST OF ACRONYMS AND SYMBOLS (Continued)

V	vanadium
V_G	gate voltage
V_D	source-drain voltage
W	tungsten
Zn	zinc

LIST OF NOMENCLATURE

C	capacitance
G	driving force
l	length of plate in contact with dielectric; total length of electrode
P	partial water vapor pressure
P_0	saturation water vapor pressure
R	gas constant
R_r	decay time
R_{RH}	resistance at relative humidity
R_0	resistance at 0% relative humidity
$R_?$	response time
s	gap between electrodes
T	temperature
w	width of plate in contact with dielectric; width of electrode facing towards dielectric
ε_r	relative permittivity
ε_0	permittivity of air
ΔC	change in capacitance
ΔR	change in resistance
ΔRH	change in relative humidity
υ_0	speed of light in a vacuum

TECHNICAL MEMORANDUM

FABRICATION AND TESTING OF A NOVEL CERAMIC-BASED ADDITIVELY MANUFACTURED HUMIDITY SENSOR

1. INTRODUCTION

1.1 Review of Current Humidity Sensors

Whether it is keeping moisture in or out of a product, a predictable atmosphere is paramount to the success of a vast range of fields. Pharmaceutical companies, refrigerators, gasoline companies, air-conditioning systems, and critical elements on the International Space Station (ISS) all rely on humidity sensors for a prediction of the ambient water content in air. Whether it is being able to predict sleep apnea in astronauts[1] or detect lethal water leakage during a spacewalk,[2] the necessity, and possibly life-saving effect, of being able to predict the ambient moisture in a local atmosphere cannot be understated. Humidity sensors that can accomplish this strenuous effort rely on the variation of three electrical properties in relation with relative humidity (RH), that is: capacitance, impedance, and thermal conductivity. The properties uniquely associated to each of these three subsets are discussed in detail below.

1.1.1 Capacitance-Based

Capacitance-based humidity sensors rely on the detection of a variation in the relative saturation, associating this to a change in relative humidity (RH) via a change in capacitance. The relation given by equation 1 represents the driving force free energy for absorption, which holds a direct impact on the capacitance readout of a sensor.

$$G = RTln\left(\frac{P}{P_0}\right) \tag{1}$$

The driving force (G) is a function of temperature (T), gas constant (R), partial water vapor pressure (P), and saturation water vapor pressure (P_0). It is then apparent that the $P \div P_0$ term must be equal to RH when the sensor is exposed to the ambient temperature of its surroundings.[3] Thus, the ambient temperature, or RH humidity holds a directly proportional relationship with the free energy available for the dielectric to absorb local water molecules. A key implication of this formula is the linear and directly proportional response RH holds on the capacitance readout of a humidity sensor.

1.1.2 Resistance-Based

Resistance-based humidity sensors operate based on measuring the amount of energy required for a proton to transition from one hydroxyl group to another, adjacent one.[4] As the concentration of protons in the hydrophilic dielectric increases, the amount of energy resisting the transfer of protons via the hopping mechanism will decrease, creating an impedance that holds an inversely proportional and exponential relationship to RH. Due to their simplicity and ease of manufacturing, resistance-based humidity sensors are cheap and commonplace in residential, commercial, and industrial environments.

1.1.3 Thermal Conductivity-Based

The core principle encompassing this sensor is the relationship between two thermistor elements measuring the difference between the conductivity of dry air and air storing water vapor. This inherently limits the sensor to a measure of absolute humidity, which is contrary to the needs of the current study. Due to this limit, the focus will be on either capacitive or resistive sensors throughout this paper.

The structures of these sensors take two general forms, with both capable of measuring either capacitance or impedance. The first and by far most common is the parallel plate capacitor (PPC) formed via the separation of two electrodes by a dielectric material, as represented in figure 1.

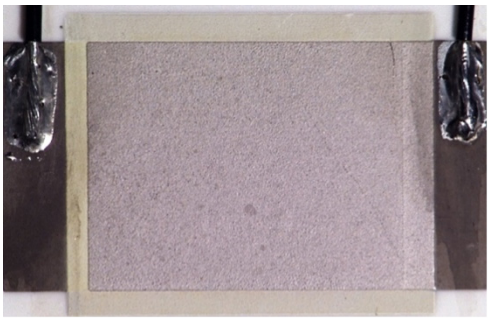

Figure 1. PPC sensor built at MSFC.

Equation 2 represents the calculation for capacitance in a PPC. Capacitance (C) is found as a function of relative permittivity (ε_r), the permittivity of air (ε_0), the width (w) and length (l) of the plate in contact with the dielectric, and gap between the electrodes (s). We can utilize this equation to provide estimates of our initial capacitance read, holding emphasis on reducing the dielectric thickness due to its inversely proportional effect on capacitance.

$$C = \frac{\epsilon_0 \epsilon_r w l}{s} \tag{2}$$

Commonplace in mass manufacturing, coplanar capacitors foster a reduction in the complexity of producing the sensor by eliminating the overlapping electrodes. As shown in figures 2 and 3, these electrodes were originally utilized extensively for non-destructive evaluation of a material (e.g., a bridge) by determining the capacitance formed via the electric field flowing through

a smooth path tracing from the anode to the cathode extending through the dielectric (in this case concrete).[5]

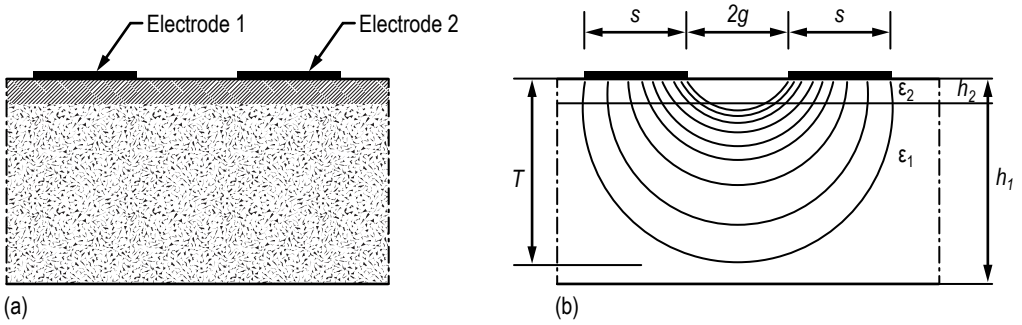

Figure 2. (a) Electrode position over the layered dielectric; (b) Electric field distribution through the dielectric material.[5]

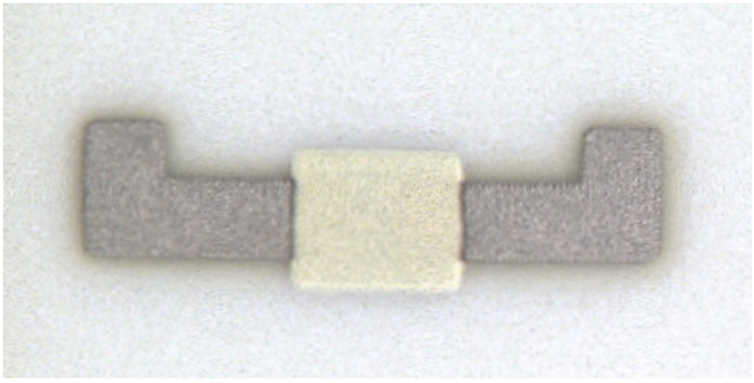

Figure 3. Coplanar electrode design built at MSFC suitable for measuring impedance or capacitance.

Capacitance between two coplanar flat electrodes is governed by the significantly more complex, piecewise Equation 3.

$$C = \frac{\epsilon_r}{377\pi v_0 \ln\left(\frac{-2}{4\sqrt{1-\frac{s^2}{(s+2w)^2}}-1}\left(4\sqrt{1-\frac{s^2}{(s+2w)^2}}+1\right)\right)} \quad for \quad 0 < \frac{s}{s+2w} \leq \frac{1}{\sqrt{2}}$$

$$C = \frac{\epsilon_r l}{120 v_0 \ln\left(\frac{-2}{\left(\sqrt{\frac{s}{s+2w}}-1\right)}\left(\sqrt{\frac{s}{s+2w}}+1\right)\right)} \quad for \quad \frac{1}{\sqrt{2}} < \frac{s}{s+2w} \leq 1 \qquad (3)$$

These equations represent C as a function of relative permittivity (ε_r), the gap between the electrodes (s), the width of the electrode facing towards the dielectric (w), speed of light in a vacuum (υ_0), and the total length of electrode (l). The directly proportional relationship between C and ε_r is obvious for both versions of the above equations. Thus, since ε_r is found as a function of the ambient RH, C must inherently depend on RH as well.

1.2 Dielectric Material Review

Fundamental to the survival and progression of the human race, sustainable energy development and storage has been identified as number 7 of the 17 goals outlined by the United Nations.[6] Ultracapacitors have routinely been identified as the missing link towards addressing this looming energy crisis. Thus, the funneling of research time and effort has been focused on the refinement of the components that make up these ultracapacitors. Characterized by equations 2 and 3, the dielectric component makes up the heart of any capacitor, inherently holding a significant impact on every electrical and physical property. As of recent, metal oxides,[7,8] perovskites,[7,9] and organic polymers[7,10] lead the charge as the primary foundation to build the dielectric from the ground up. Each class contains its advantages and disadvantages, represented in table 1.[7]

Table 1. Various sensing media.[7]

Sensing Material	Time (s)		Humidity Range (%)	Working Voltage	Sensitivity	
	$R_?$(s)	R_r(s)			Definition	Value
1. Metal oxides						
SnO_2/SBA-15	15	21	11–98	AC 1 V	–	–
$SnWO_4-SnO_2$	30	100	5–98	–	R_0/R_{RH}	22,386
$K_{0.5}Na_{0.5}NbO_3$	8	18	11–95	AC 1 V	–	–
K^+•Doped $SnO_2-LiZnVO_4$	80	100	33–93	AC 1 V	–	–
2. Organic polymers						
MPOSS	3	40	11–95	AC 1 V	–	–
3. Oxygenated salt						
$BaTiO_3$ Nanofibers	30	9	11–95	DC 15 V	–	–
$ZnSnO_3$	7	16	11–97	AC 1 V	$\Delta R/\Delta RH$	1.04 %/RH%
4. Sulfide						
MoS_2	10	60	0–35	V_G 30 V V_D 1 V	$(R_{RH}-R_0/R_0)$	10,000
5. Halide perovskite						
$CH_3NH_3PbI_{0.2}Cl_{25}$	24	24	35–65	DC 2 V	R_0/R_{RH}	1,422
$Cs_2BiAgBr_6$	1.78	0.45	15–78	AC 1 V	$(R_{RH}-R_0/R_0)$	1,162
$CsPb_2Br_5-BaTiO_3$	5	5	25–95	AC 1 V	$\Delta C/\Delta RH$	21,426 pF/RH%
$CsPbBr_3$ nanoparticles	2.8	9.7	11–95	AC 0.02 V	$\Delta R/\Delta RH$	1.5565 %/RH%

A ceramic material in the perovskite family was developed by NASA Marshall Space Flight Center (MSFC), referred to as reduced lanthanum barium titanate (rLBT). rLBT is comprised of reduced barium titanate ($BaTiO_3$) doped with lanthanum (La) and co-doped with potassium

hydroxide (KOH). Figure 4 provides a diagram of the structure of $BaTiO_3$ used in the creation of rLBT. It was found that rLBT exhibited an enormously high ε_r value in the range of $\approx 10^5$.[11–13] However, it is known that these "giant ultracapacitor properties"[13] are not so easy to control. For instance, an unexpected characteristic of extreme sensitivity to moisture was discovered, which shifted the focus of the team at NASA toward the use of rLBT as a highly efficient, vapor-sensitive dielectric.[12] Proven effective even at a minute thickness of 30 μm, the drastically reduced environmental footprint of the sensor enabled it for use in monitoring respiration in previously impossible areas, such as space suits.[1] This study also found that the fast recovery rates were under 1 s for a step change of 63% RH; in other words, for an instantaneous RH change from 30% to 93%, the capacitance readout would change and then stabilize within 1 s. This discovery qualified it for use in quickly detecting volatile vapors in critical environments like the ISS,[2] while also inherently enabling it for use in fields dependent on quick moisture reactions (e.g., detection of sleep apnea via breathing patterns).[1]

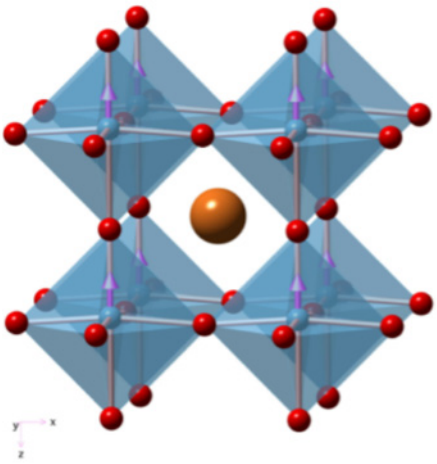

Figure 4. Structure of $BaTiO_3$.[14]

Current formation of a dielectric based on rLBT is an extensive process, entailing multiple cumbersome steps: First, a mixture of lanthanum hydroxide, barium oxide, and titanium dioxide, with particle diameters between 50–700 nm, are heated in a range of 1,000–1,300 °C.[15] This process generates a sintered mixture which then requires a complex regiment to create a printable form. This form incorporates a mix of glass particles, surfactants, solvents, organic vehicles, binders, and co-dopants. The liquid mixture is deposited onto a substrate via a screen-printing method like that used in the printing of semiconductors. Once deposited, extensive processing is required to remove the liquid portions of the mixture.[15] Routinely, processing necessitates cycling between heating at 850–900 °C and cooling in a nitrogen atmosphere. These cumbersome final steps inherently limit the ability to mass manufacture sensors based on rLBT. This research aims to utilize advancements in additive manufacturing (AM) to create a humidity sensor that can eliminate the inconvenient final high temperature firing stages currently necessary, replacing them with a simple cure either under low heat (<110 °C) for epoxy or under ultraviolet (UV) light for UV-sensitive resin.

2. rLBT GENERATION SELECTION

Two different iterations of the La-doped rLBT base were studied. A batch developed in 2018 was processed at a maximum sintering temperature of 1,150 °C,[15] while the latest development was processed at a temperature in excess of 1,250 °C. The former batch also utilized larger precursor particles as opposed to the latter, where much smaller particles were used. These different firing ranges and particle sizes led to obvious physical changes in the properties of the base powder. The 1,150 °C samples exhibited a blueish shade, while the 1,250 °C samples showcased a more off-white tint, as represented in figures 5–6 below.

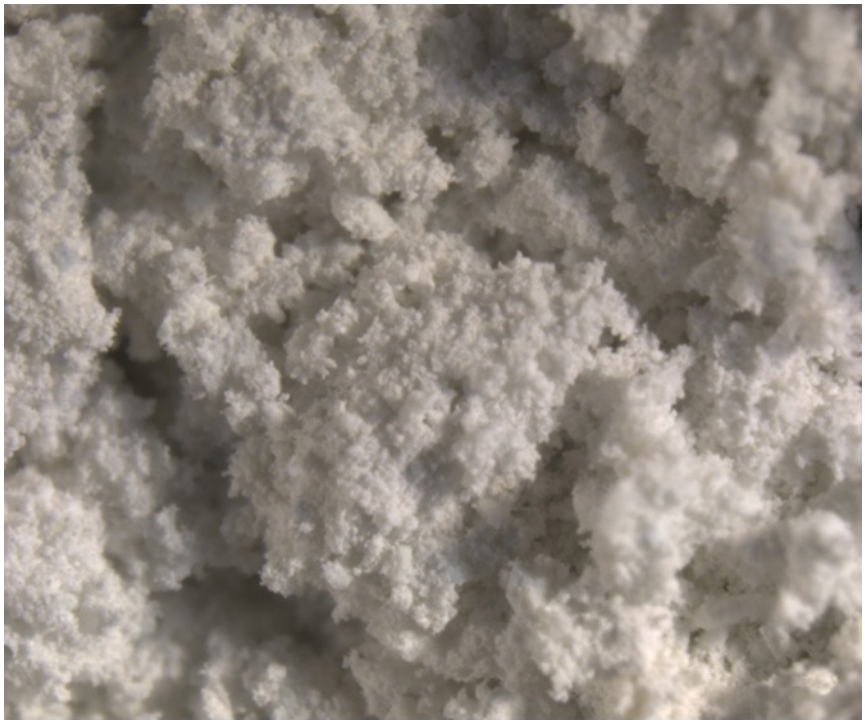

Figure 5. 1,150 °C Sample.

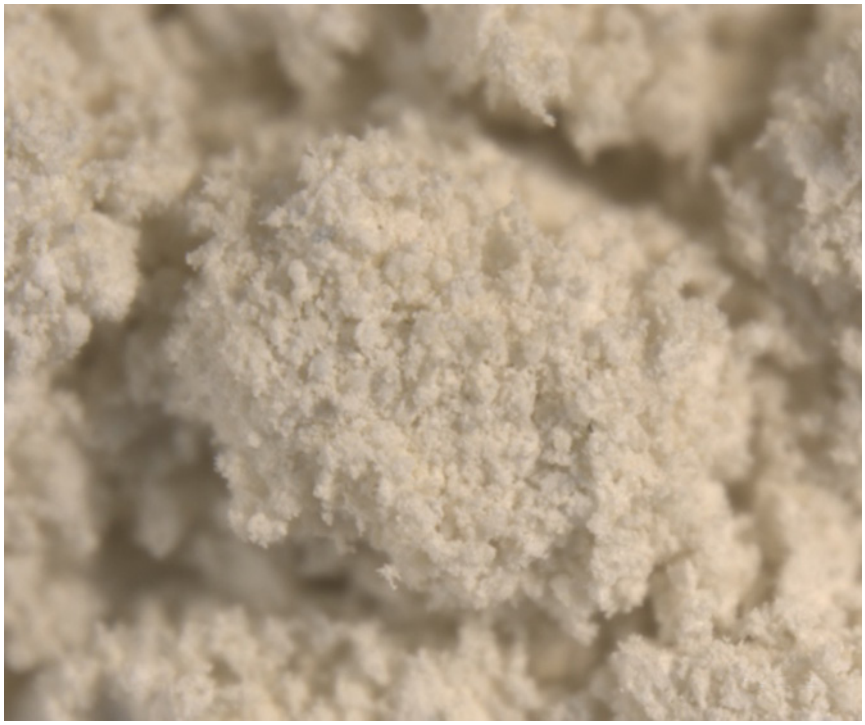

Figure 6. 1,250 °C Sample.

2.1 Binder Choice

Adhesion of local rLBT particle clusters is paramount to enabling the formation of networks that foster the communication of electrons across the dielectric. Liquid binders capable of extreme loading, upwards of 3–4 times their relative wt.%, help to 'glue' these particle clusters together. The properties of a selected liquid binder were found to hold significant effects on the mechanical and electrical properties of the final dielectrics. Due to this, the outcomes of two binders are presented: UV-curable resin and epoxy.

A commercial 3D Eco UV-curable resin from Shenzhen Anycubic Technology Company was chosen due to its ease of use and availability. Selectively curable resin inherently enables the reduction of cumbersome, prior necessary stages, by meshing together these stages into one process. In example, fabrication of current rLBT sensors require drying at 250 °C for each layer of dielectric added followed by a burn off at 850 °C to remove all organics from the material. The selected UV-curable resin completely removes this step, replacing it with a simple cure under a 400–450 nm UV light. Despite the ease of use, meeting of the percolation threshold was challenging for this material.

Difficulties in meeting percolation led the authors towards the use of a new binder, one with a known trait of higher loading capacity: epoxy. Epoxy's long heritage in various fields enables easy application towards the tested case of a binder for the ceramic rLBT particles. The specific epoxy used in the creation of the tested rLBT sensors was EpoThin™ two-part resin epoxy. Post-test analysis of the epoxy-based samples confirmed a significant increase in the range of output capacitance. Intuitively, it is thought that an increase in the weight ratio of rLBT with respect to a binder

would lead the final solution to hold properties more similar to the rLBT. Thus, the authors sought an additive that could help accomplish this.

2.2 Surfactant Characteristics

He, Xu, and Ji utilized a dispersant additive to modify the rheological properties of a ceramic slurry, resulting in a positive effect on the loading of ceramic in the binder.[16] This insight led to the use of anionic surfactants, particularly Stepan Stepfac™ 8180 and Ashland Dextrol™ OC-40, to reduce the surface tension in hopes of increasing the wt.% of the dissolved rLBT particles. Both Stepfac 8180 and OC-40 are tridecyl alcohol ethoxylate phosphate esters. Immediately after use of either surfactant, a notable hysteresis drift for the UV-curable resin-based samples was produced and is represented by the plots shown in Figures 7–9. Epoxy-based samples exhibited no drift (see figure 10) and were influenced much less by the incorporation of Stepfac 8180, as revealed in figure 11.

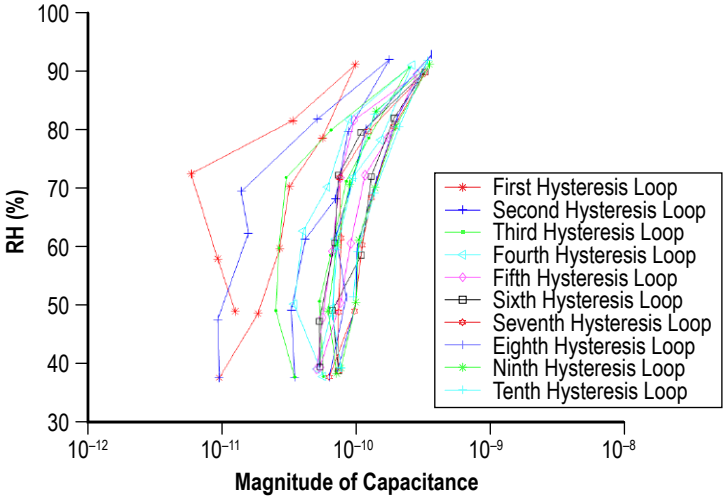

Figure 7. Control: UV-curable resin with OC-40 measured at a frequency of 25 Hz.

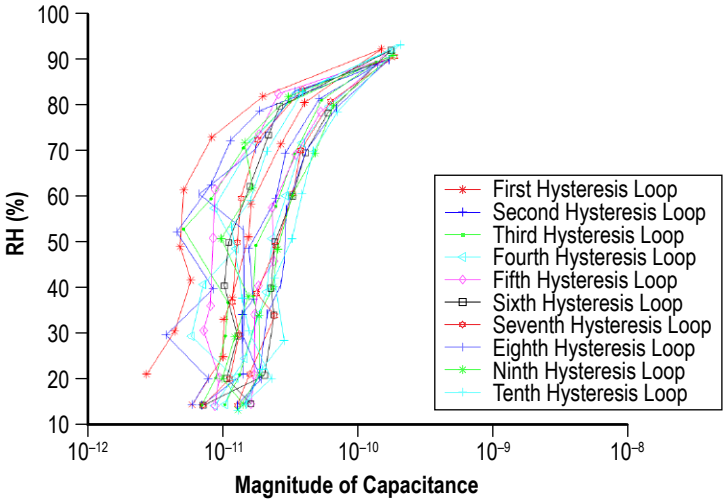

Figure 8. Control: UV-curable resin with Stepfac 8180 measured at a frequency of 25 Hz.

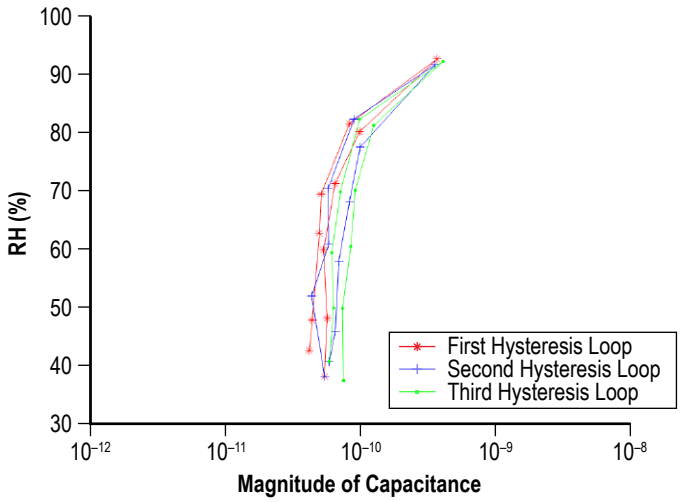

Figure 9. Control: UV-curable resin measured at a frequency of 25 Hz.

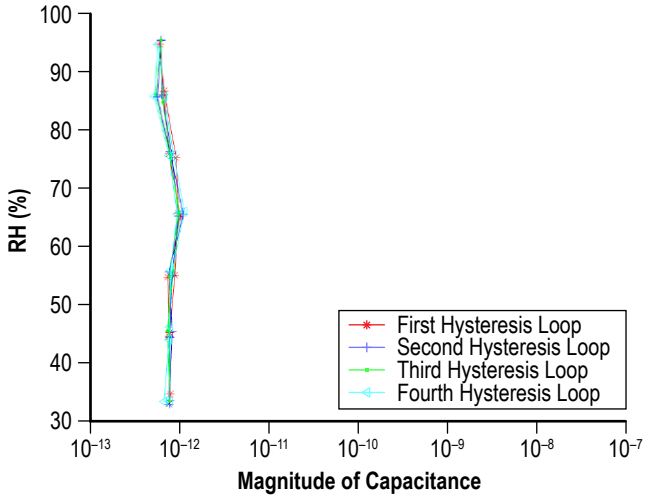

Figure 10. Control: Epoxy measured at a frequency of 20 Hz.

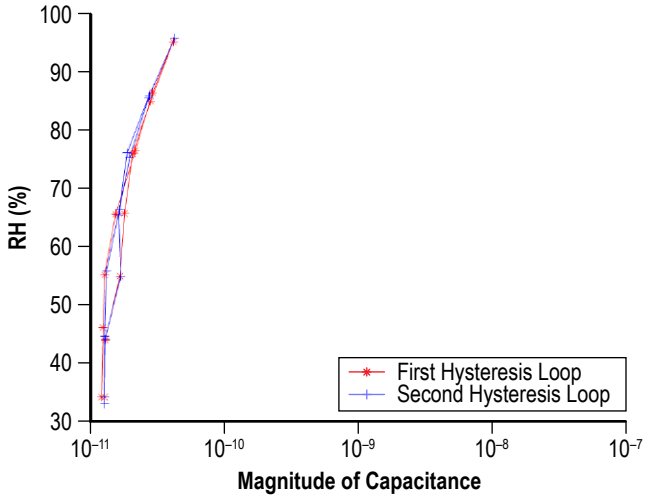

Figure 11. Control: Epoxy with Stepfac 8180 measured at a frequency of 30 Hz.

Predicting and manipulating the hysteresis drift was highly dependent on several factors. Particularly, the step times between humidity changes and the local ambient temperature were found to hold the most noteworthy effect.[17] Thus, these two variables were highly controlled during the duration of the testing. For all presented results in this study, an ambient room temperature of 25 °C was held in the humidity chamber. Still, OC-40 exhibited a tendency to drift at much higher rates than Stepfac 8180. As such, the use of Stepfac 8180 for the primary choice of surfactant can be found through all samples.

An unintuitive result, confirmed multiple times through various sensor iterations, was that samples created solely from the selected UV-curable resin exhibited a much higher hysteresis drift tendency than samples mixed with Stepfac 8180. This surprising result is present for both generations of rLBT, showcased in the plots in Figures 12–15.

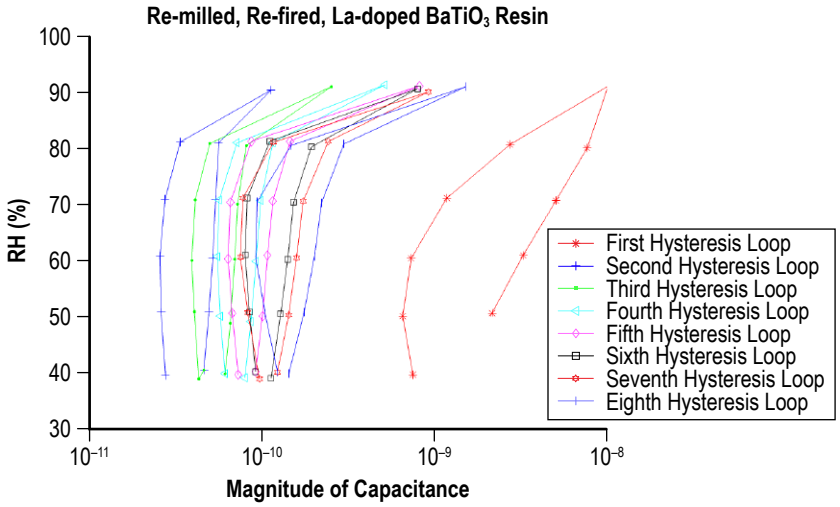

Figure 12. Base fired at 1,150 °C without surfactant measured at a frequency of 20 Hz.

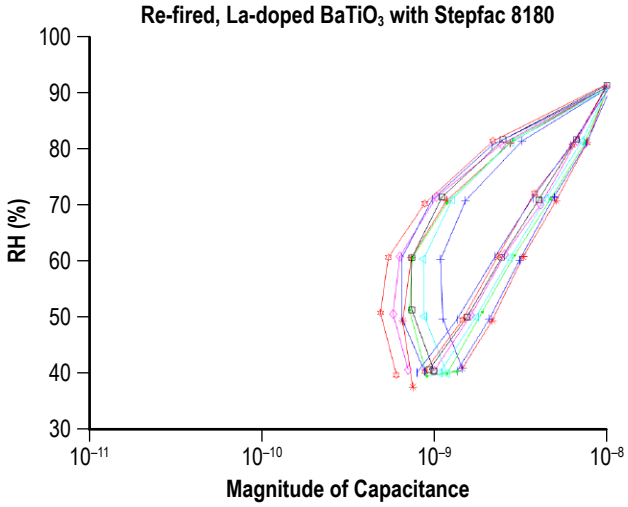

Figure 13. Base fired at 1,150 °C with surfactant measured at a frequency of 20 Hz.

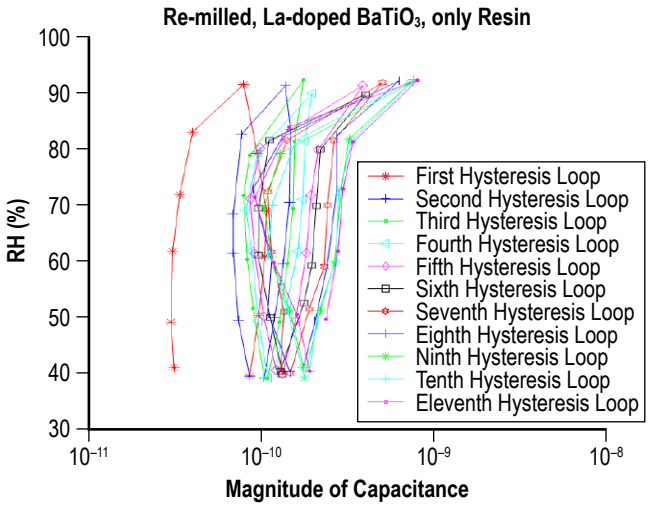

Figure 14. Base fired at 1,250 °C without surfactant measured at a frequency of 25 Hz.

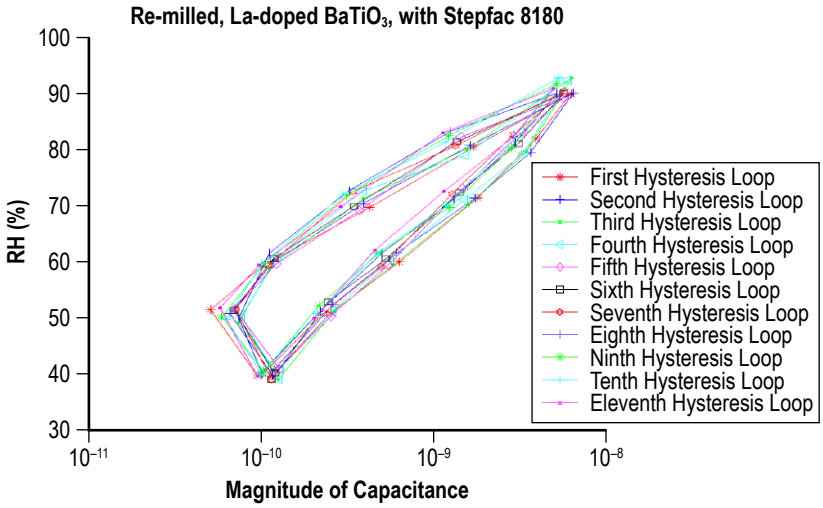

Figure 15. Base fired at 1,250 °C with surfactant measured at a frequency of 25 Hz.

The previous effect of surfactant held in UV resin samples immediately faded away for all epoxy tests. In fact, the behavior of the samples seemed nearly independent with regards to surfactant wt.%. This is shown in figure 16 comparing four of the tested epoxy-based samples.

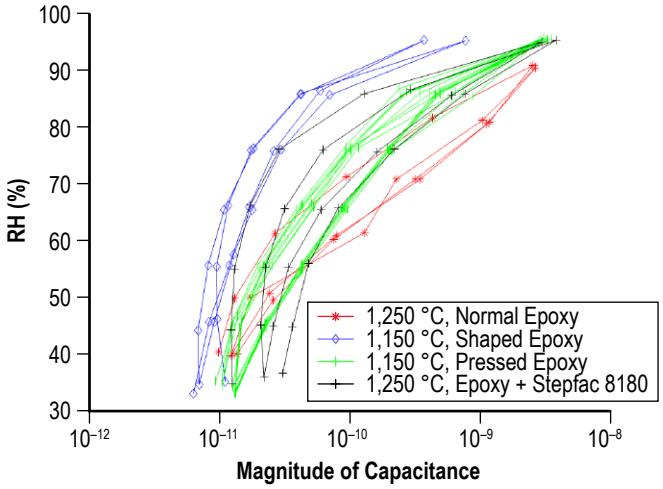

Figure 16. Comparison of epoxy samples measured at a frequency of 25 Hz.

The preceding samples fabricated from epoxy utilized different generations of rLBT base. A notable difference in the dielectric thickness was observed spanning across the different generations. Insight through the sensors studied proved this variation in thickness to hold influence on the ability of the dielectric to release the encapsulated water molecules when the RH retreated. This data is captured in Table 2. Another prominent difference between the two samples is that the 1,150 °C samples contain a slightly higher $BaTiO_3$ wt.% in comparison to the 1,250 °C sample. With a difference of only 0.3 wt.%, a significant difference in the structure of the cured dielectric is presented through figures 17–20.

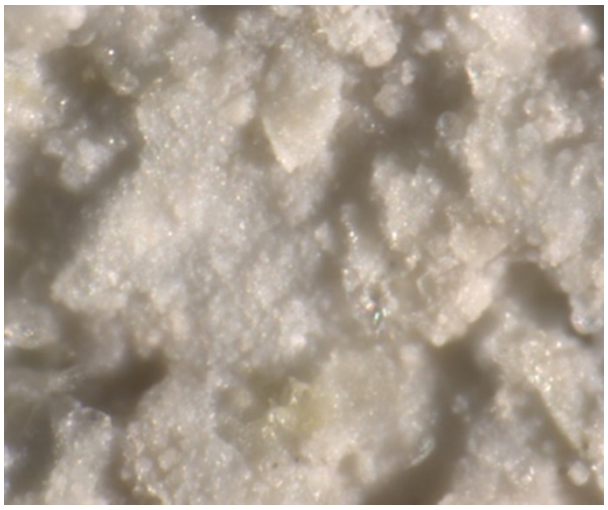

Figure 17. Structure of particle clusters in epoxy sample fired at 1,150 °C.

Figure 18. Epoxy sample with material fired at 1,150 °C.

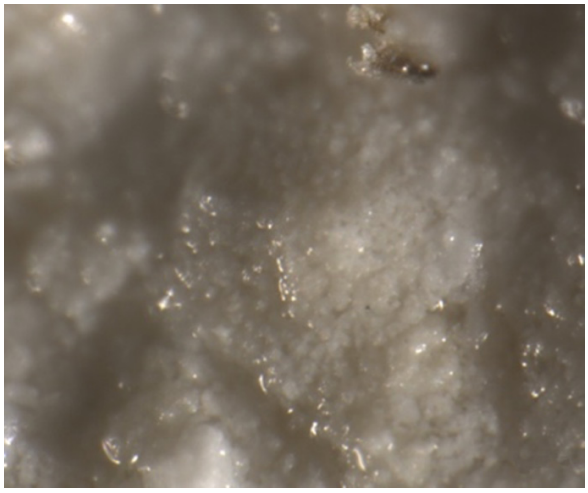

Figure 19. Structure of particle clusters in epoxy sample fired at 1,250 °C.

Figure 20. Epoxy sample with material fired at 1,250 °C.

Table 2. Tested sensors.

	Material	Weight Ratio	Response	Hysteresis Drift	Outstanding Notes	Step Time (m)	Dielectric Thickness
UV-curable Resin	Resin	N/A	1 OM	Slight drift	–	10	400 µm
	Resin + OC-40	1.244 R: 1 O	1 OM	Rapid drift at beginning, coalesce towards end	–	10	320 µm
	Resin + Stepfac 8180	1.244 R: 1 S	1.1 OM	Exact same as OC-40	–	10	340 µm
	CD (1 layer) (R + S)(1,250 °C)	2.63 B : 1 R	1 OM	Rapid drift at beginning, coalesce towards end	More cream in color	5	460 µm
	CD (2 layer) (R + S)(1,250 °C)	2.63 B : 1 R	1 OM	Rapid drift at beginning, coalesce towards end	Notable difference in texture	5	350 µm
	CD (3 layer) (R + S)(1,250 °C)	2.63 B : 1 R	1 OM	Rapid drift through entirety of testing	More cream in color	5	390 µm
	MD (R)(1,250 °C)	2.88 B : 1 R	0.9 OM	Rapid drift at beginning, coalesce towards end	Similar size as the 1-layer dielectric	25	970 µm
	MD (R + S)(1,250 °C)	2.81 B : 1 R + S	2 OM	No noticeable drift	Flattened prior to testing	25	290 µm
	MD (R)(1,150 °C)	2.29 B : 1 R	1 OM	Rapid drift at beginning, coalesce towards end	Powder was deoxidized in 2019	N/A	420 µm
	MD (R + S)(1,150 °C)	2.4 B : 1 R + S	3.1 OM	Moderate drift at beginning, coalesce towards end	Powder was deoxidized in 2019	N/A	380 µm
	MD (R + S)(1,150 °C)	2.2 B : 1 R + S	2.7 OM	Slight drift, coalesce towards end	22 rLBT: Stepfac, stamped	15	290 µm
	MD (R + S)(1,150 °C)	2.2 B : 1 R + S	2.1 OM	Slight drift, coalesce towards end	22 rLBT: Stepfac	15	340 µm
	FD (R)(1,150 °C)	2.23 B : 1 R	1.2 OM	Consistent drift	Flattened prior to testing	15	460 µm
	FD (R + S)(1,150 °C)	2.37 B : 1 R + S	1.4 OM	Consistent drift	Flattened prior to testing	15	190 µm
	FF (R + S)(1,150 °C)	1.9 B : 1 R + S	2.8 OM	No noticeable drift	22 rLBT: Stepfac, stamped	15	240 µm
	FF (R + S)(1,150 °C)	1.9 B : 1 R + S	2.9 OM	No noticeable drift	22 rLBT: Stepfac	15	340 µm
	MD & FD (R)(1,150 °C)	2.43 B : 1 R	2 OM	Extreme drift through duration of testing	Sample was shaped to electrode	15	420 µm
Epoxy	Epoxy	N/A	0.1 OM	No noticeable drift	Formed with Kapton® tape	15	230 µm
	Epoxy + Stepfac 8180	2.04 E : 1 S	0.2 OM	No noticeable drift	Formed with Kapton tape	15	90 µm
	Final rLBT (E)(1,250 °C)(1)	2.4 B : 1 E	3 OM	Slight drift, coalesce towards end	Slightly different slope below	15	280 µm
	Final rLBT (E)(1,250 °C)(2)	2.4 B : 1 E	3 OM	Slight drift, coalesce towards end	RH vs. capacitance matched perfectly for samples 2, 3, and 4	15	270 µm
	Final rLBT (E)(1,250 °C)(3)	2.4 B : 1 E	3 OM	Slight drift, coalesce towards end		15	260 – 290 µm
	Final rLBT (E)(1,250 °C)(4)	2.4 B : 1 E	3 OM	Slight drift, coalesce towards end		15	270 µm
	Final rLBT (E)(1,250 °C)(Kap)	2.1 B : 1 E	2.3 OM	Less drift than the above final sensors	Formed with Kapton tape	15	350 µm
	MD (E)(1,250 °C)	2.15 B : 1 E	2.5 OM	No noticeable drift	Near log-linear output	25	1,180 µm
	MD (E + S)(1,250 °C)	2.14 B : 1 E + S	2.5 OM	No noticeable drift	Rapid increase in (*C*) for lower RH	10	440 µm
	MD & FD (E)(1,250 °C)	2.15 B : 1 E	2 OM	Slight drift, coalesce towards end	Formed with Kapton tape	15	N/A
	MD & FD (E)(1,150 °C)	2.43 B : 1 E	2.2 OM	No noticeable drift	Rapid increase in (*C*) for lower RH	15	280 µm
	PD, MD & FD (E)(1,150 °C)	2.43 B : 1 E	2.6 OM	No noticeable drift	Flattened prior to testing	15	250 µm
	FF (E)(1,150 °C)(Thin)	1.24 B : 1 E	2.5 OM	Less drift than the above sensors	Formed with Kapton tape	15	150 µm

3. FABRICATION OF SENSORS

Refinement in the production of semiconductors has been critical in the rise of electrical devices. The use of screen printing to mass manufacture these semiconducting materials has branched to various fields, one of which is the fabrication of sensors with repeatable properties and characteristics.[15] Samples for this research were fabricated through a procedure derived from the methods utilized by Rolin and Small;[15] Weng et al.;[9] and Qi et al..[18] A premixed slurry was forced over a controlled aperture, displacing the uncured dielectric onto the electrode below it. Using the alternative binders discussed in section 2.1 enabled the elimination of high-temperature postprocessing steps that were necessary in previously established methods. As a result, UV-curable resin samples were processed with a simple 60 s cure under a 20 W, 400–450 nm UV light, while epoxy-based sensors were subjected to a low-heat (<120 °C) drying period ranging from 30 m to 2 h. The general steps used to produce a sensor for this research, as compared to the steps established in Rolin and Small,[15] are shown in figure 21.

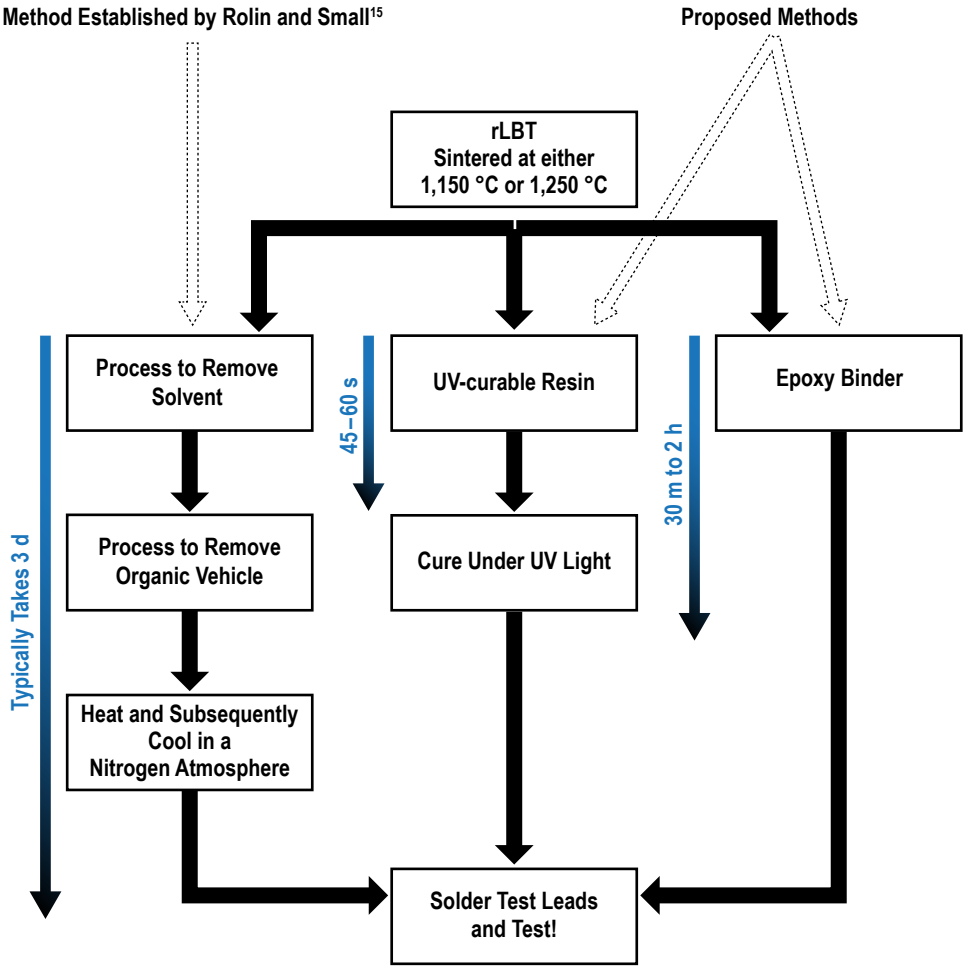

Figure 21. Reduction in processing with novel methods.

While the samples produced from the UV-curable resin exhibited a decent response of two orders of magnitude, the overall better characteristics and reduced equipment requirements of the epoxy binder led the authors to fabricate the final sensors entirely derived from epoxy. The previously-presented independence of the epoxy-based humidity sensors' performance toward the use of Stepfac 8180 meant that the final sensors produced without the surfactant required less processing, further reducing the start to finish manufacturing time. The decision between electrodes based on a typical parallel plate capacitor design or a coplanar design relied heavily on minimizing the complexity and required manufacturing necessary to produce reliable humidity sensors. As represented throughout industry,[3] the coplanar design eliminates several steps required by parallel electrodes; thus the choice of coplanar electrodes will be found throughout all presented sensors. The choice of which generation of humidity sensing powder utilized required a much more extensive testing regime, spanning tens of iterations with each iteration containing up to four samples each.

Though the physical differences found between the rLBT powders sintered at 1,150 °C and 1,250 °C are prominent, their electric-magnetic properties withhold obvious variances. The data obtained indicated that the powder sintered at 1,250 °C may lead to a more log-linear RH vs capacitance, which was previously explained to be more favorable due to simplification of the required regression analysis necessary to output a valid readout. Thus the 1,250 °C rLBT was chosen to fabricate the final sensors pictured in figures 22–25.

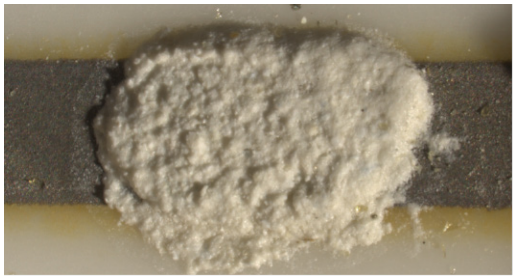

Figure 22. Final Sensor 1.

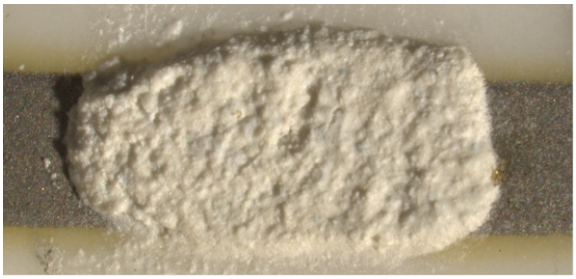

Figure 23. Final Sensor 2.

Figure 24. Final Sensor 3.

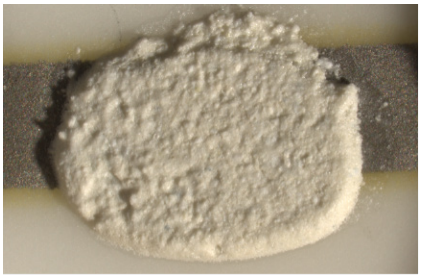

Figure 25. Final Sensor 4.

Production of the final sensors was designed to match known techniques common in the art of semiconductor manufacturing with hopes of fostering an ease of future adaption towards the production of the presented sensors. The specific steps used to produce the final sensor selection were as follows:

(1) A solution of EpoThin epoxy was formed with a resin-to-hardener weight ratio of 5:1, as recommended by the manufacturer.

(2) The epoxy was mixed with a premeasured amount of 2 wt.% KOH with La-doped $BaTiO_3$ base, sintered at 1,250 °C, to reach the desired rLBT-to-epoxy weight ratio of 2.4:1.

(3) The rLBT/epoxy mixture was then displaced over the coplanar electrodes in a method similar to that of screen printing. Due to the heavy loading of rLBT in the epoxy, the final solution was extremely viscous, reducing the chance of settling or migration once displaced onto the dielectric.

(4) The wet sensor was left out at room temperature to cure for ≈2 h or heated with a basic hotplate at 110 °C to reduce the time of total solidification to ≈30 m.

4. RESULTS AND ANALYSIS

The exhibited final sensor selection showcased the best range, spanning three orders of magnitude for a step change in 60% RH. This impressive range was also followed by the expected near log-linear output, with sensors 2, 3, and 4 showing a near-exact yield in capacitance across the tested RH range. The slight deviation found in sample 1 is believed to be due to the dielectric's marginally thicker height. The output of each sensor and a comparison of all sensors is presented in figures 26–30.

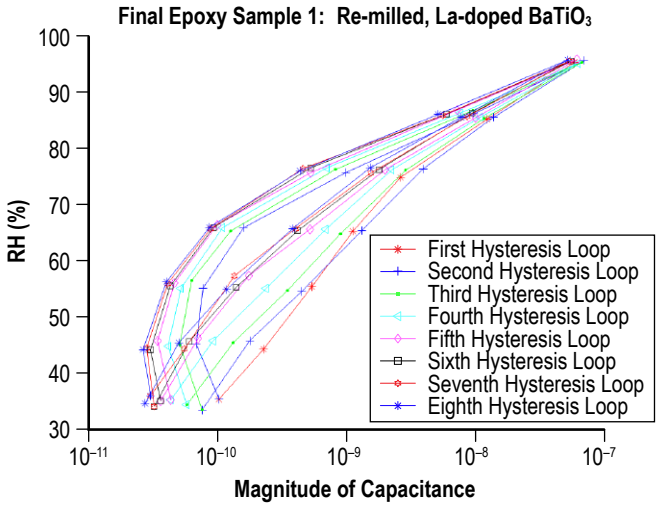

Figure 26. Final Sample 1, RH vs Capacitance. Base fired at 1,250 °C and measured at a frequency of 20 Hz.

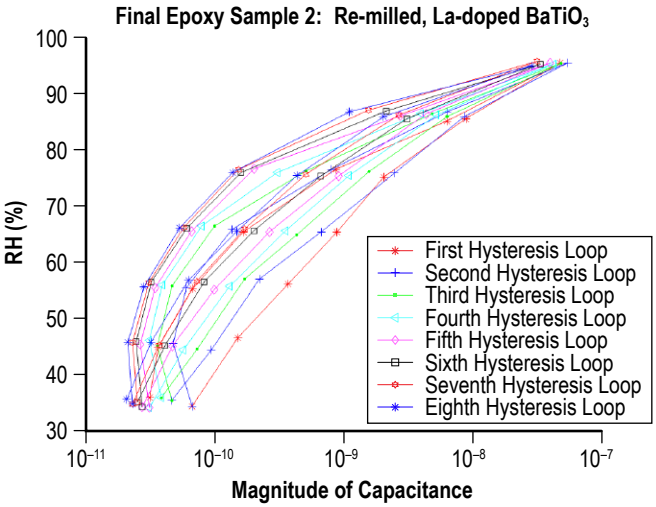

Figure 27. Final Sample 2, RH vs Capacitance. Base fired at 1,250 °C and measured at a frequency of 20 Hz.

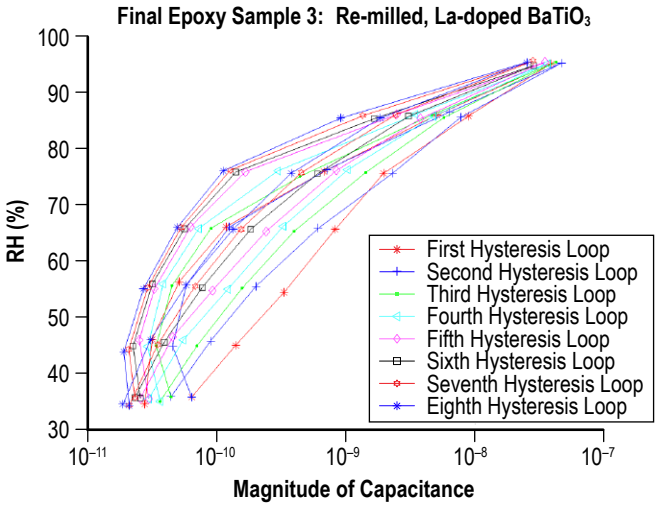

Figure 28. Final Sample 3, RH vs Capacitance. Base fired at 1,250 °C and measured at a frequency of 20 Hz.

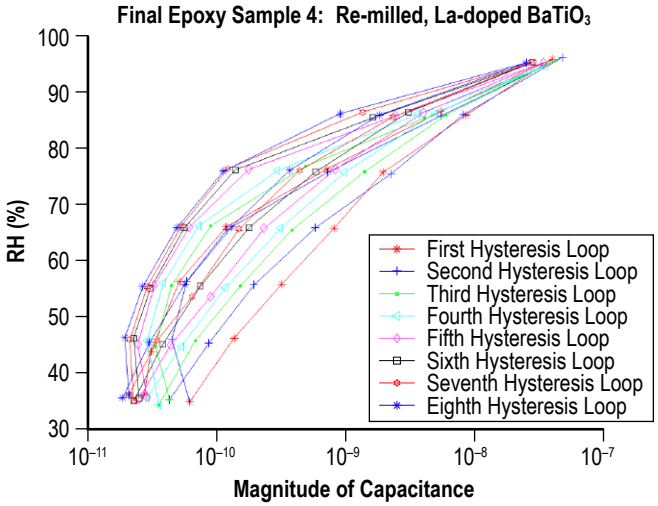

Figure 29. Final Sample 4, RH vs Capacitance. Base fired at 1,250 °C and measured at a frequency of 20 Hz.

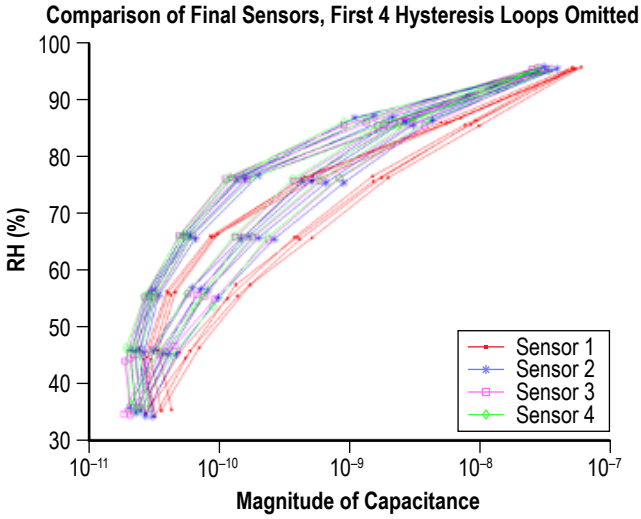

Figure 30. Comparison of the final sensors. Base fired at 1,250 °C and measured at a frequency of 20 Hz.

Samples produced from epoxy were extremely durable, resisting shearing off even when attempting to leverage a scalpel underneath the dielectric. A vastly improved resistance to hysteresis drift found across all generations of rLBT bases was extremely favorable and led to steady output for all tested loops. The samples fabricated from the 1,250 °C powder also showcased a near log-linear response, which would make calibration easier for analog processors.

5. CONCLUSIONS

The core of this research was to extend the already proven and published screen-printed sensor[11–13,15] via the use of either an epoxy or UV-curable resin binder. Accomplishment of this goal enabled a drastic reduction in the total required production time, while reducing the parts and machines necessary to manufacture a viable sensor. Both UV-curable resin-based and epoxy-based sensors held similar ranges in capacitance as the cited screen-printed sensor, as displayed in the comparison found in figure 31. Several industries may be impacted by the drastically improved durability granted through epoxy's binding strength, such as high-temperature applications in aerospace environments.

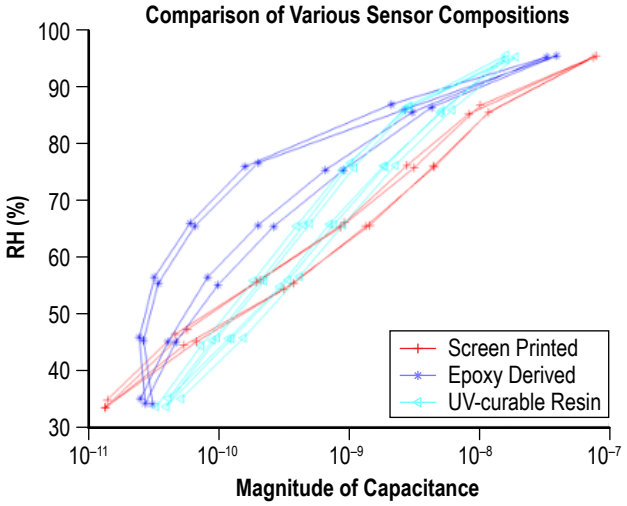

Figure 31. Comparison of various sensor configurations. Base fired at 1,250 °C and measured at a frequency of 20 Hz.

Several important insights were gained through the months spent developing this AM humidity sensor. The importance of meeting the percolation network for sufficient communication across the ceramic slurry cannot be understated. Thus, the authors recommend future testing of additives that can enhance the amount of rLBT dissolved in the binder. This study only analyzed the effects of surfactants Stepfac 8180 and OC-40; but as He, Ju, and Ji pointed out, "typical surfactants such as polyvinylpyrrolidone K10, polyvinylpyrrolidone K15 and oleic acid"[16] can also be used to increase the loading of a ceramic-based material into a binder. An additive that enhances the communication of the $BaTiO_3$ particles across the solution may also increase the range of capacitance for a select range of RH. Initial insight leads to the thought of polyvinylidene fluoride to accomplish this due to its resistance to solvents, acids, and hydrocarbons.[19] In addition, a more finely-milled rLBT and a more refined mixing mechanism, such as ultrasonics, may lead to a higher rLBT-to-binder weight ratio.

REFERENCES

1. Small, I.K.; Jovanov, E.; and Rolin, T.D.: "Monitoring of Respiration by Means of an Additively Manufactured Barium Titanate-based Hygroscopic Sensor," Paper Presented at 2019 IEEE SoutheastCon, Huntsville, AL, April 11–14, 2019, 5 pp., doi:10.1109/SoutheastCon42311.2019.9020362.

2. Meyer, N.; and Bartush, M.: "NASA's Space Suit: A Maintenance Study," Paper Presented at 2018 Annual Reliability and Maintainability Symposium (RAMS), Reno, NV, January 22–25, 2018, 5 pp., doi:10.1109/RAM.2018.8463132.

3. Wilson, J. S.: "CHAPTER 12 – Humidity Sensors," in *Sensor Technology Handbook*, 1st ed., Elsevier, Burlington, MA, pp. 271–280, 2005.

4. Tripathy, A.: Pramanik, S.:, Manna, A.; et al.: "Uniformly Porous Nanocrystalline $CaMgFe_{1.33}Ti_3O_{12}$ Ceramic Derived Electro-Ceramic Nanocomposite for Impedance Type Humidity Sensor," *Sensors,* Vol. 16, No. 12, p. 2029, 18 pp., doi:10.3390/s16122029, November 2016.

5. Nassr, A.A.; Ahmed, W.H.; and El-Dakhakhni, W.W.: "Coplanar Capacitance Sensors for Detecting Water Intrusion in Composite Structures," *Measurement Science and Technology*, Vol. 19, No. 7, p. 075702, 7 pp., doi:10.1088/0957-0233/19/7/075702, July 2008.

6. United Nations: "Energy — United Nations Sustainable Development," <https://www.un.org/sustainabledevelopment/energy/>, July 25, 2022.

7. Wu, Z.; Yang, J.; Sun, X.; et al.: "An Excellent Impedance-Type Humidity Sensor Based on Halide Perovskite $CsPbBr_3$ Nanoparticles for Human Respiration Monitoring," *Sensors and Actuators B: Chemical*, Vol. 337, No. 12, p. 129772, doi:10.1016/j.snb.2021.129772, March 2021.

8. Tomer, V.K.; and Duhan, S.: "In-situ Synthesis of SnO_2/SBA-15 Hybrid Nanocomposite as Highly Efficient Humidity Sensor," *Sensors and Actuators B: Chemical,* Vol. 212, pp. 517–525, doi:10.1016/j.snb.2015.02.054, June 2015.

9. Weng, Z.; Qin, J.; Umar, A.A.; et al.: "Lead-Free $Cs_2BiAgBr_6$ Double Perovskite-Based Humidity Sensor with Superfast Recovery Time," *Advanced Functional Materials,* Vol. 29, No. 24, p. 1902234, doi:10.1002/adfm.201902234, June 2019.

10. Dai, J.; Zhang, T.; Zhao, H.; and Fei, T.: "Preparation of Organic-Inorganic Hybrid Polymers and Their Humidity Sensing Properties," *Sensors and Actuators B: Chemical,* Vol. 242, pp. 1108–1114, doi:10.1016/j.snb.2016.09.139, April 2017.

11. Tucker, D.S.; Rolin, T.D.; and Hill, C.W.: U.S. Patent No. 11,230,501, January 25, 2022.

12. Sherrard, C.G.; and Rolin, T.D.: "Solid State Ultracapacitor Polymer Composite," NASA/TM–20220018181, NASA Marshall Space Flight Center, Huntsville, AL, 30 pp., December 2022.

13. Cortés-Peña, A.Y.; Rolin, T.D.; Strickland, S.M.; and Hill, C.W.: (2017, August). "A Novel Solid State Ultracapacitor," NASA/TM—2017–219686, NASA Marshall Space Flight Center, Huntsville, AL, 44 pp., August 2017.

14. Qaisar, S.A.: "Fatigue and High Temperature Behaviour of the La-doped Bismuth-Ferrite Lead-Titanate System," Ph.D. Thesis, University of Leeds, Leeds, UK, 176 pp., September 2013.

15. Rolin, T.D.; and Small, I.K.: U.S. Patent 9,987,658, June 5, 2018.

16. He, X.; Xu, J.; and Ji, W.: "The Effect of Surfactants on the Performances of Ceramic Slurry by Material Extrusion and Photo-Polymerization Combined Molding Process," *Journal of the Ceramic Society of Japan*, Vol. 129, No. 8, pp. 489–495, doi:10.2109/jcersj2.21057, August 2021.

17. Rotronic: "The Capacitive Humidity Sensor," <https://www.rotronic.com/media/productattachments/files/c/a/capacitive_humidity_sensor_final.pdf>, 2021.

18. Qi, Q.; Zhang, T.; Yu, Q.; et al.: "Properties of Humidity Sensing ZnO Nanorods-base Sensor Fabricated by Screen-printing," *Sensors and Actuators B: Chemical*, Vol. 133, No. 2, pp. 638–643, doi:10.1016/j.snb.2008.03.035, August 2008.

19. Kang, G.-D.; and Cao, Y.-M.: "Application and Modification of Poly(Vinylidene Fluoride) (PVDF) Membranes – A review," *Journal of Membrane Science*, Vol. 463, pp. 145–165, doi:10.1016/j.memsci.2014.03.055, August 2014.

20. Kim, Y.; Jung, B.; Lee, H.; et al.: "Capacitive Humidity Sensor Design Based on Anodic Aluminum Oxide," *Sensors and Actuators B: Chemical*, Vol. 141, No. 2, pp. 441–446, doi:10.1016/j.snb.2009.07.007, September 2009.

21. Al-Ta'ii, H.; Amin, Y.; and Periasamy, V: "Humidity Influenced Capacitance and Resistance of an Al/DNA/Al Schottky Diode Irradiated by Alpha Particles," *Scientific Reports,* Vol. 6, p. 25519, doi:10.1038/srep25519, May 2016.

National Aeronautics and
Space Administration
IS63
George C. Marshall Space Flight Center
Huntsville, Alabama 35812